Light-scattering-induced artifacts in a complex polymer gel dosimetry phantom

Stephen G. Bosi,[1,2,*] Pourandokht Naseri,[2] and Clive Baldock[2]

[1]Department of Radiation Oncology, Prince of Wales Hospital, Randwick NSW 2031, Australia

[2]Institute of Medical Physics, School of Physics, University of Sydney, Sydney NSW 2006, Australia

*Corresponding author: s.bosi@physics.usyd.edu.au

Received 21 November 2008; accepted 24 February 2009;
posted 20 March 2009 (Doc. ID 104301); published 22 April 2009

Certain polymer gels become turbid on exposure to ionizing radiation, a property exploited in medical dosimetry to produce three-dimensional dose maps for radiotherapy. These maps can be read using optical computed tomography (CT). A test phantom of complex shape ("layered tube") was developed to investigate the optical properties of polymer gel dosimeters when read using optical CT. Extinction coefficient profiles from tomographically reconstructed slices of the phantom exhibited several artifacts. A simple model invoking scattered light in the gel was able to account for all artifacts, which in a real dosimeter may have been mistaken for other phenomena, resulting in incorrect readings of dose.

OCIS codes: 120.3890, 170.6960, 290.2648.

1. Introduction

The term "gel dosimetry" [1] refers to a growing class of techniques in which radiation-sensitive gels are used to measure radiation dose, usually for medical applications. Gels are designed so that one or more properties (e.g., x-ray attenuation [2], optical attenuation, [3], proton spin relaxation [4], or acoustic properties [5]) vary monotonically (preferably linearly) with radiation dose. This allows one or more of the commonly used medical imaging modalities (x-ray or optical computed tomography [CT], magnetic resonance imaging or ultrasound) to be used to measure a three-dimensional (3D) map of radiation dose within the gel. Such a 3D technique has potential advantages over more established two-dimensional (2D) techniques, such as radiographic film, in verifying the complex radiation fields produced by modern radiotherapy techniques such as intensity-modulated radiotherapy [6].

Gels based on aqueous media are desirable because they have a composition and electron density similar to human tissue and so are highly "tissue equivalent" with respect to their radiation attenuation properties [7,8]. This is important in medical dosimetry, as this is the principle factor determining the extent to which the dose map in the dosimeter mimics that in a patient subject to the same treatment.

If the gel's optical transmittance changes with dose, then optical CT [3,9–13], the optical analogue of x-ray CT, can be used to extract a 3D map of optical extinction coefficient Δ and hence (if calibrated) radiation dose. It is a relatively inexpensive 3D imaging modality developed mainly for reading dosimetric gels.

There are two main optical CT configurations. Successive 2D spatial maps of gel transmittance can be read either by using a scanning laser beam or by acquiring transmission images using a CCD camera. In both cases, the dosimeter is rotated around a single axis, and 2D transmission projections are acquired for hundreds of orientations. Conventional CT reconstruction algorithms can then be used to recreate a 3D map of the optical extinction coefficient.

The pioneering Fricke dosimeter [14] exploits the fact that, in specially prepared solutions, Fe^{2+}

0003-6935/09/132427-08$15.00/0

is oxidized quantitatively to Fe^{3+} by exposure to ionizing radiation. The addition of xylenol orange to a gel containing Fricke solution renders this chemical change visible [15], the gel's optical absorbance increasing with dose, allowing the use of optical methods to read the dose map [16]. However, being water soluble, Fe^{2+} and Fe^{3+} ions (responsible for the color change) diffuse rapidly through the gel [17,18], degrading the 3D dose map over time, thus limiting the allowable time between exposure and reading.

Developed to overcome diffusion, "polymer gels" [4,19], for example, polyacrylamide gel (PAG) [20] or polyacrylamide gelatin and tetrakis (PAGAT), [21] exhibit microscopic regions of radiation-induced polymerization and cross linking (Fig. 1), which cause a dose-dependent change in opacity (or extinction coefficient Δ) via optical scattering. These polymerized regions are tangled in the network moiety of the gel, and so they do not diffuse, making the gel more stable, allowing more time to acquire the dose map [22]. However, unlike Fricke gels, scattering rather than absorption is responsible for optical extinction, which complicates the optical behavior of the gel.

For small to moderate degrees of polymerization, optical extinction in optically scattering polymer gels should obey the venerable Bouguer–Lambert law:

$$T = \exp(-d\,\Delta), \tag{1}$$

where T is optical transmittance, d is path length, and Δ is the extinction coefficient. Moreover, if the size and spatial distribution of scattering centers is incoherent, then, for small to moderate degrees of polymerization, Δ should be proportional to concentration of scattering centers hence radiation dose [3]. In conditions where Δ is proportional to concentration, Eq. (1) is commonly known as the Beer–Lambert law. For larger doses, various phenomena can cause the relationship between Δ and dose to deviate from linear. For example, the degree of polymerization in the dosimeter can become saturated at high dose [20].

However, purely optical effects can also contribute. For example, forward single-scattered or multiple-scattered stray light can indirectly enter the detector [23] resulting in an underestimate of Δ. Given that the granular structures in the polymerized gel [Fig. 1(b)] have dimensions ranging from below the wavelength of light (λ) to several times λ, a more detailed and quantitative discussion would need to invoke a scattering theory (such as Mie theory) that includes the effects of interference/diffraction.

There are also other more subtle effects, such as coherence in the distribution of scattering centers and changes in the mean refractive index as the degree of polymerization increases, but as will be shown later, stray light is able to account for virtually all the deviation observed here.

Some polymer gels can exhibit nonlinear behavior even at low dose, for example, with respect to their magnetic resonance properties [24], but this is not necessarily reflected in their Δ values [3,25].

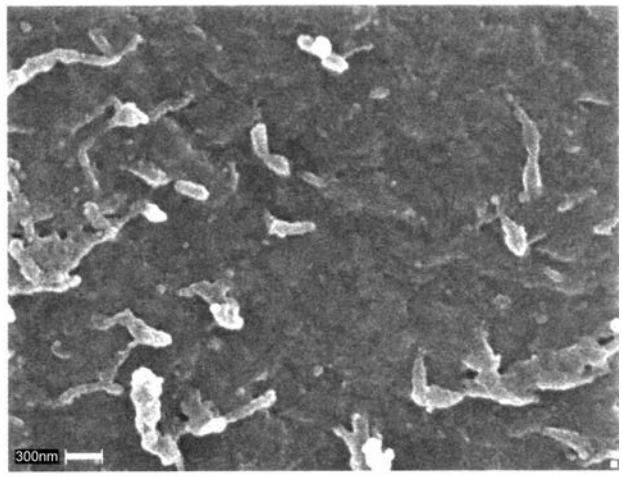

(a)

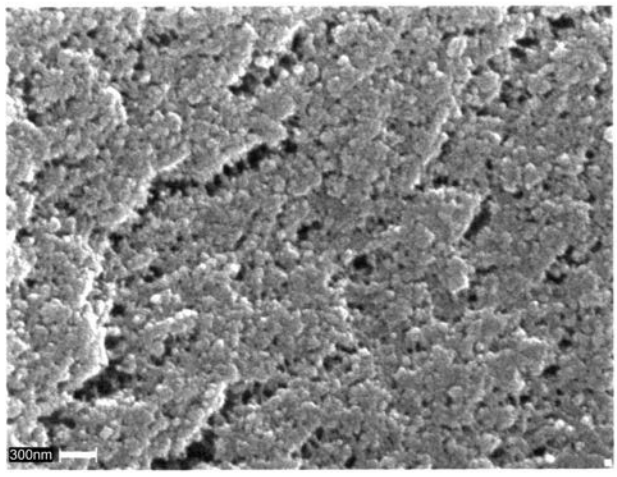

(b)

Fig. 1. Scanning electron microscope images of PAG gel (a) unexposed and (b) exposed to 25 Gy of photons from a clinical linear accelerator operating at 6 MV. Compare the smooth consistency of (a) with the granular texture in (b) due to polymerization and cross linking after exposure. The size of both scale bars is 300 nm. Specimen preparation: fixed in OsO_4, dehydrated, critical-point-dried, then cut.

In an earlier paper [25], a radiation-inert, layered finger gel phantom was developed to investigate optical scattering artifacts in gels subject to optical CT. The antiseptic Dettol (Reckitt Benckiser) was added to porcine gelatin to simulate the opalescence (or Tyndall scattering) typical of an exposed polymer gel dosimeter. Differing doses were simulated by varying the concentration of the antiseptic. This allowed the study of purely optical artifacts affecting optical CT of turbid gels, uncomplicated by true non-uniformities and nonlinearities caused by the behavior of a real dosimeter irradiated by a real clinical radiation beam. In a follow-up of that paper [26], the effect of varying path length within a funnel-shaped

scattering phantom of uniform turbidity was examined.

In those papers [25,26], it was shown that stray light caused two closely related artifacts: first, CCD cone beam optical CT *underestimates* larger Δ values, and second, a "dishing" (or "cupping") artifact is observed. In the latter effect, profiles in regions of known uniform Δ yield plots of Δ versus position, which deviate from an ideal plateau by dipping down in the central region to form the shape of a dish.

Dishing occurs because, for the longest light paths, true transmittance is lower than for short path lengths, so stray light represents a larger fraction of the signal measured by the CCD (hence an apparent enhancement of transmittance). In a back-projection reconstruction, the central voxels are reconstructed mainly from transmittance data near the central axis of the projections that have the longest path lengths. Consequently, Δ toward the center of a highly turbid region is underestimated more severely than at the periphery.

The following research extends the earlier finger phantom work by examining these effects in a more complex phantom: the "layered tube" phantom. The work is motivated by the need to understand the limitations of polymer gel dosimeters and to develop models for correcting these artifacts. However, some aspects of these effects would also have analogues in imaging modalities such as x-ray CT.

2. Experimental Procedure and Data Analysis

A. The Scanner

The phantom was imaged using a CCD-camera-based cone beam optical CT scanner [27] (Vista Scanner, Modus Medical Devices Inc.). The scanner was originally developed for use with optically absorbing Fricke gels but can also be used with optically scattering polymer gels. The scanner (Fig. 2) consists of a spatially extended, narrow-wavelength range diffuse light source, illuminating (in transmission) a gel dosimeter contained in a cylindrical 9.5 cm diameter by 13 cm high screw-top polyethylene terephthalate (PETE) vessel (supplied with the scanner). The dosimeter is mounted in a water-filled aquarium (to match the refractive index of the dosimeter, thereby cancelling refractive distortion). The dosimeter is rotated incrementally while a CCD camera fitted with a narrow-wavelength filter (633 nm in this case) collects transmission projection images [e.g., Fig. 3(a)]. A 3D map of Δ [Fig. 4(a)] is then reconstructed using the supplied software (VistaRecon) that employs the Feldkamp back-projection algorithm [28]. In this work, 512 projections were employed, and the resolution of the reconstruction was 0.25 mm × 0.25 mm × 0.25 mm per voxel.

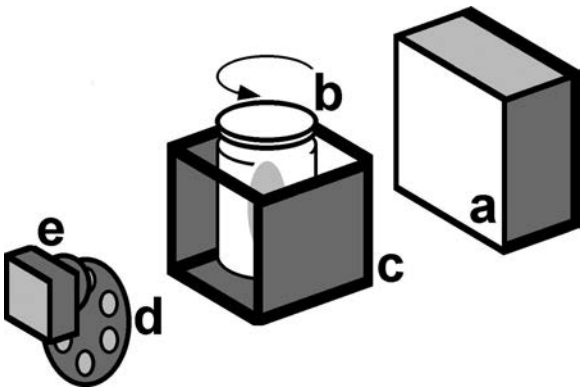

Fig. 2. Vista cone beam optical CT scanner (Modus Medical Devices Inc.). (a) Spatially extended light source with diffusing panel, (b) dosimeter mounted in a rotating clamp, (c) aquarium containing index matching liquid, (d) optical filter wheel, and (e) CCD camera.

B. The Phantom

The layered tube phantom [Fig. 3(a)] was constructed using a method similar to that developed for the Dettol layered finger phantom [25], and 300 bloom porcine gelatin powder and water were mixed in the proportions 52.6 to 1000 g to produce the pure "base gelatin" corresponding to a "zero dose" gel. Differing amounts of Dettol were then added to aliquots of the base gelatin to produce gels of varying Δ.

The phantom (contained in one of the PETE vessels) consisted of an outer mantle of base gelatin surrounding a central, vertical cavity ("tube region") of a nominally 15 mm outer radius. The tube region was backfilled with nine horizontal layers, each 10 mm thick of graduated Δ, the uppermost layer having the lowest antiseptic concentration (and Δ). In the earlier finger phantom, a 10 mg/g mixture of neat Dettol liquid in base gelatin was found to simulate an increase in Δ equivalent to that of a PAGAT gel exposed to around 8.3 Gy of ^{60}Co gamma photons, so the most turbid layer here is roughly equivalent to 12 Gy, although these figures are very rough and will depend on the precise formulation of the gel.

Running through the center of the tube region was a narrower cylindrical cavity of a roughly 8 mm radius ("pith region"), which was then backfilled with base gelatin. Two test tubes of different diameter were used successively as internal molds to create these cylindrical cavities during preparation.

Inclusion of the "zero dose" central pith simulates a radiotherapy treatment, where a high dose region surrounds a low dose region (for example, when treating around the spine where ensuring a low dose to the sensitive spinal cord is essential).

For gel dosimetry, optical CT requires measurement of the gel dosimeter in both the exposed and unexposed states to establish the reference baseline Δ, so a second, reference phantom was made consisting of an identical PETE vessel filled entirely with base gelatin, having the same Δ as the mantle and pith regions (Fig. 5) of the layered tube phantom.

The layered tube phantom (the "specimen" phantom) and the base gelatin baseline reference phantom (the "reference" phantom) were scanned using the

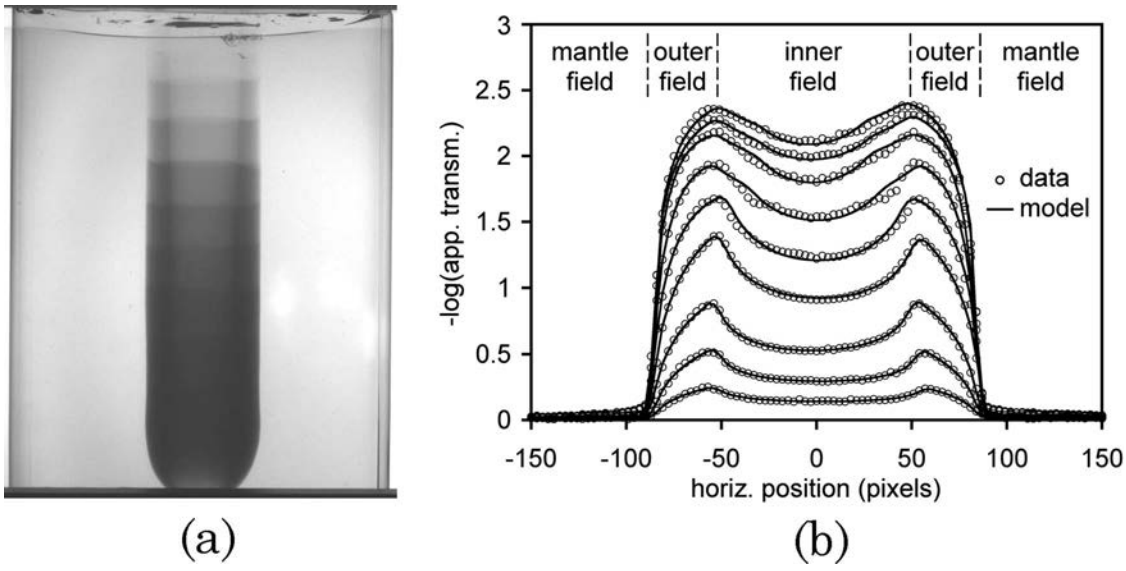

Fig. 3. Layered tube phantom. (a) Raw transmission projection image of the phantom. (b) Horizontal profiles of apparent transmittance through successive layers of a projection image (reference baseline corrected), both experimental and modeled. The lowermost plot represents the top layer of the phantom. For clarity, only one-third of the experimental points are plotted. The boundaries between the inner, outer, and mantle fields within the horizontal profiles of the 2D projection image are identified.

optical CT scanner. Sets of projections [such as Fig. 3 (a)] were then reconstructed using the software accompanying the scanner (VistaRecon) to produce a 3D map of Δ [Fig. 4(a)], and radial profiles of Δ [Fig. 4 (b)] within each layer of the reconstruction were extracted using ImageJ (open source Java-based image analysis application, National Institutes of Health).

A model (the Bouguer–Lambert plus stray light model) based on those used for the earlier Dettol phantoms [25,26] was applied to baseline reference corrected projection transmittance profiles [shown on a negative log scale in Fig. 3(b)].

C. The Model

Light received by the scanner camera was assumed to consist of two components: directly transmitted light (obeying the Bouguer–Lambert law [Eq. (1)]) and stray light scattered back into the camera indirectly.

The intensity of the stray light along horizontal lines of pixels in the 2D projection images was assumed to be horizontally uniform (but not vertically) within the boundaries of each of the 2D fields defined in Figs. 3(b) and 5 (namely, the "outer," "inner," and "mantle" fields). This is an avowedly

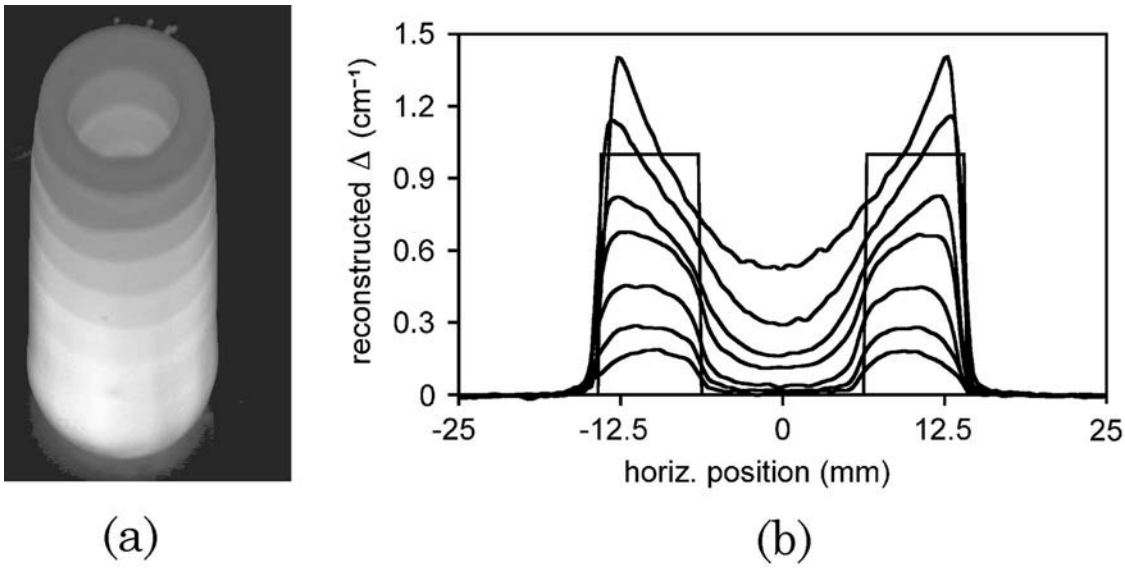

Fig. 4. (a) Rendered image of the layered tube phantom reconstruction. Darker pixels denote lower extinction coefficient Δ. (b) Extinction coefficient profiles along radial horizontal lines through several layers within the reconstruction. Ideally, all profiles should resemble the shape of the overlaid twin rectangular plateaus (apart from height).

simplified but quite a good assumption [25,26] that accounts well for the artifacts evident here. The success of this assumption is probably a consequence of the simple geometry and highly symmetric nature of the phantom. It also seems likely that the randomness of the spatial distribution and broadness of the size distribution of the scattering particles were large enough to minimize any strong angle dependence of the stray light component.

For horizontal profiles through a projection image, the (apparent) transmittances of the mantle (T_{mantle}), outer (T_{outer}), and inner (T_{inner}) fields were assumed to be of the forms

$$T_{\text{ref}}(x,y) = \exp(-d_{\text{ref}}(x)\Delta_B) + S_{\text{ref}}(y), \quad (2)$$

$$T_{\text{mantle}}(x,y) = [\exp(-d_7(x)\Delta_B) + S_7(y)]/T_{\text{ref}}(x,y), \quad (3)$$

$$\begin{aligned} T_{\text{outer}}(x,y) = {} & [\exp(-d_6(x)\Delta_B) + S_6(y)] \\ & \times [\exp(-d_4(x)\Delta_{\text{tube}}(y)) + S_4(y)] \\ & \times [\exp(-d_5(x)\Delta_B) + S_5(y)]/T_{\text{ref}}(x,y), \end{aligned} \quad (4)$$

$$\begin{aligned} T_{\text{inner}}(x,y) = {} & [\exp(-d_6(x)\Delta_B) + S_6(y)] \\ & \times [\exp(-d_3(x)\Delta_{\text{tube}}(y)) + S_3(y)] \\ & \times [\exp(-d_1(x)\Delta_B) + S_1(y)] \\ & \times [\exp(-d_2(x)\Delta_{\text{tube}}(y)) + S_2(y)] \\ & \times [\exp(-d_5(x)\Delta_B) + S_5(y)]/T_{\text{ref}}(x,y), \end{aligned} \quad (5)$$

where x and y are, respectively, the horizontal and vertical coordinates on projection images, $T_{\text{ref}}(x,y)$ is the transmittance of the reference phantom, Δ_{tube} and Δ_B are, respectively, the extinction coefficients of the tube region and the base gelatin. S_{ref} and S_1 to S_7 are the stray-light-induced increases in apparent transmittance through the reference phantom and the specimen phantom regions 1–7, respectively (see Fig. 5). d_{ref} and d_1 to d_7 are, respectively, the light path lengths through the reference phantom and the specimen phantom regions 1–7. By symmetry, ideally $d_2 = d_3$ and $d_5 = d_6$. Small deviations from these symmetries in the real phantom were ignored.

Horizontal line intensity profiles through the raw specimen phantom 2D projection images were plotted. These were divided by corresponding line profiles through the reference phantom projections to yield (apparent) transmittance profiles. The negative logarithms of these data are plotted as discrete points in Fig. 3(b). A model plot [unbroken curves in Fig. 3(b)] for each experimental profile was then generated using the stray light model. These model profiles were fitted to the experimental data very closely using least squares regression, yielding fitted values for the diameter of the pith, ideal Δ, and stray light

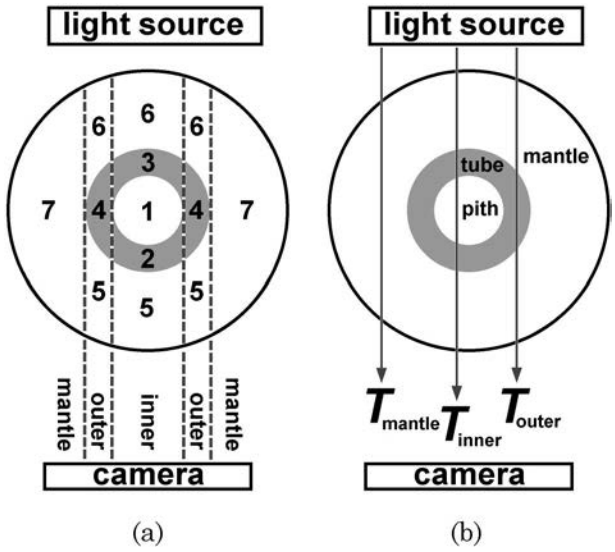

Fig. 5. Top views of 3D regions within the volume of the layered tube phantom marked with the region labels used in Eqs. (2)–(5). Also shown are example optical paths used to calculate model transmittances through the three distinct 2D fields (inner, outer, and mantle) within each layer of a reference baseline corrected projection image.

intensities within each of the seven labeled regions in Fig. 5 for planes through each of the nine horizontal layers of the tube.

The extinction coefficient Δ_B for the base gelatin (i.e., used for the reference, mantle, and pith gels) was first obtained by fitting the stray light model to the mantle field of the apparent transmittance profiles [using Eqs. (2) and (3)]. To avoid the possibility of sloppy overfitting, the number of adjustable parameters in the tube region was reduced by obtaining the mean of Δ_B values (after exclusion of two very poor outliers) obtained from fits to 11 different heights within the mantle field. This single *fixed* value was then used in all subsequent model fits to the tube region.

This Δ_B value was then subtracted from the subsequently fitted extinction coefficient value within each layer of the tube region (Δ_{tube}) in order to convert them to baseline corrected values for comparison with the Δ_{tube} values obtained from the reconstruction (both plotted in Fig. 6).

The phenomenon of scattering, however, has another effect in addition to producing stray light. It also causes boundaries in transmission images to appear more diffuse. Sharp boundaries between adjacent fields in the projection images are smoothed out into a penumbra. Equations (2)–(5) nominally assume that both stray light intensity and transmittance make a stepwise transition at a field boundary. The assumption of horizontal uniformity of stray light intensity within a field is expected to be least valid within the penumbra near boundaries of the fields defined in Figs. 3 and 5. The assumption of stepwise transitions across boundaries results in unrealistic spikes and cusps at boundaries. To mitigate

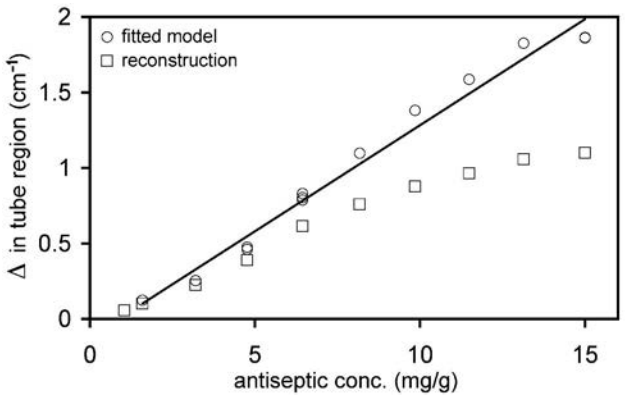

Fig. 6. Baseline subtracted extinction coefficients within successive layers of the tube region Δ_{tube} versus concentration of antiseptic (w/w) derived from the reconstruction and from fits to transmittance profiles taken from reference baseline corrected projection images using the Bouguer–Lambert plus stray light model. The straight line is fitted to the Δ_{tube} values derived from the model.

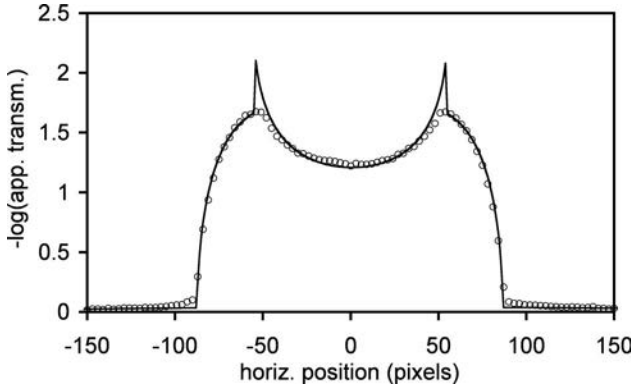

Fig. 7. Example of a fit with smoothing (seven-point moving average) and spike truncation disabled to reveal an example of severe boundary spikes. Note that away from the spikes, the model still fits well. Only one-third of the points are plotted.

these spikes, the model transmittance profiles were smoothed using a seven-point moving average prior to evaluating the sum-of-squares penalty function in the regression fitting. The same smoothing window was used for all layers being analyzed.

In the four layers with largest Δ, across the boundary between the inner and outer fields, the transitions in transmittance and stray light intensity assumed by the model were most severe, and diffuseness of the real penumbra was most pronounced. In these cases, the seven-point moving average alone was not sufficient to completely mitigate the spurious spikes (Fig. 7) in the model, so in these four layers, across this boundary, the spikes were truncated and the model transmittance profiles interpolated linearly before evaluation of the sum-of-squares penalty function. Because this truncation/interpolation extended only into the inner field (subtending the pith region) and not the outer field (containing the wings of the tube region) in Fig. 3(b), this should have a minimal effect on the fitted Δ_{tube} values plotted in Fig. 6 (circular plot points).

This was confirmed by performing one of the fits with and without this truncation. In the untruncated case, during fitting the penalty function residuals were given zero weighting within the untruncated spikes. The difference between the two fitted Δ_{tube} values was not discernible to the eye when plotted in Fig. 6.

3. Results and Discussion

The Δ values obtained from the 3D reconstruction are reference baseline subtracted, so ideally these plots [Fig. 4(b)] should be uniform and nonzero within the tube region and zero within the mantle and pith regions. An example of an ideal plot (with two rectangular plateaus) is overlaid in Fig. 4(b). All the plots should have this shape (although varying in height). Clearly these data, especially those of highest Δ, exhibit serious deviations from ideal.

Consistent with observations in the earlier layered finger phantom [25], the tube region is dished—concave upward, especially in layers of highest antiseptic concentration. Depending on the irradiation geometry, had this effect been observed in a real polymer gel in a clinical photon beam, it may have been incorrectly interpreted as "beam hardening"—lower energy x-ray photons being attenuated preferentially, resulting in a beam increasing in mean energy (and hence enhanced "penetrating power") with depth. No such effect can happen here, not even optically. Because the scanning is conducted using narrow-wavelength-band light, there will be no artifacts due to wavelength dependence of scattering.

Δ, averaged over a horizontal slice within each layer of the tube region of the reconstruction, were then plotted (Fig. 6 square plot symbols) against concentration (expressed as milligrams of neat Dettol liquid per gram of the mixed gel). Because of stray light, higher Δ values are being underestimated, so instead of an ideal linear plot, it starts to saturate at high concentration, also consistent with observations in the earlier phantom. Had this been observed in a real polymer gel dosimeter, it would have been difficult to distinguish from saturation of polymerization. Had this saturation been real, deviations from linearity could be corrected by simply using the dose response curve as a "lookup table" or calibration curve.

In contrast with the earlier Dettol phantoms [25,26], however, an additional artifact is evident. Within the nominally "zero dose" pith region, which should exhibit a baseline corrected extinction coefficient of zero, an effect opposite to that in the tube region is observed; Δ is *overestimated*, and this effect becomes increasingly severe with increasing antiseptic concentration (and Δ) in the nearest layer of the tube region surrounding the pith (Fig. 8). Therefore the lookup table approach to correction of nonlinearity would not work for an optically scattering system such as this, because the degree of nonlinearity (and

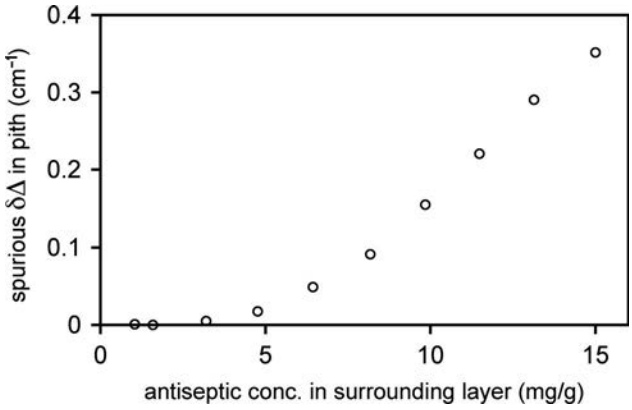

Fig. 8. Spurious elevation $\delta\Delta$ of extinction coefficient (derived from the reconstruction) within the pith region versus concentration of antiseptic (w/w) in the nearest layer of the surrounding tube region.

even its sign) is geometry dependent, and so such a simpleminded correction would lead to incorrect dose readings in the clinic.

As an indication of the clinical significance of this effect, using the rough "calibration" described in Subsection 2.B, the spurious elevation of Δ within the pith is equivalent to roughly 2 Gy in the section surrounded by the most turbid layer of the tube.

Spurious elevation of pith Δ occurs because, for extremely opaque layers of the tube, stray light in the mantle region in front of the tube (Region 5) will dominate the detected signal, so negligible information about the pith will be detected, and so the apparent behavior of Δ in the pith region will tend toward the reconstructed behavior of Δ in the tube (i.e., larger than background and dished). For intermediate, more transmitting layers, the relative effect of the stray light will be reduced, so the apparent Δ of the pith will reduce, tending toward its true background value (zero) for the least opaque layers of the tube.

The "Bouguer–Lambert plus stray light" model closely fits the experimental transmittance plots [Fig. 3(b)]. Moreover, the plot of fitted Δ in the tube region versus antiseptic concentration (Fig. 6 circular plot symbols) is close to an ideal linear relationship, supporting the idea that, for Δ_{tube} taken from the reconstructed data, the observed deviation from linearity can be accounted for almost entirely by the presence of stray light.

The model assumes that directly transmitted light obeys Bouguer–Lambert law, but it does not explicitly assume that the extinction coefficient is proportional to concentration of scattering centers, so the fact that this proportionality is evident in Fig. 6 is not a consequence of bias toward the in-built assumptions of the model, but rather it reinforces the model's physical plausibility.

It should be pointed out that, in Fig. 6, both the experimental and the model values of Δ_{tube} extrapolate to zero at a nonzero antiseptic concentration. This is to be expected. The scattering centers responsible for the turbidity are suspended droplets of oils (from the antiseptic) that are sparingly soluble in aqueous media. At (nonzero) concentrations below the solubility limit of those oils, there will be no scattering centers. Therefore using the mass of added antiseptic as a proxy for concentration of scattering centers results in a small offset in concentration.

The simple, uniform stray light assumption works well for the simple, symmetric geometric shapes used here. However, for handling more complicated, realistic dose profiles, a reconstruction algorithm utilizing a more complex scattering model needs to be developed, perhaps involving an optical Monte Carlo algorithm based on Mie scattering theory or algorithms based on optical diffusion similar to those employed in diffuse optical tomography [29,30]. Because of the similarity between optical and x-ray cone beam CT, algorithms used to correct similar artifacts in x-ray CT could be adapted to the optical case (see the mini review in [31]).

Scanning systems can also be designed to be less sensitive to stray light. Optical CT systems based on scanning with a laser beam (instead of being flood illuminated as in a cone beam CCD system) will produce less stray light because a much smaller volume of the dosimeter is being illuminated at any given time, but generally speaking these are much slower than CCD cone beam systems. Faster designs are being developed, however (see, for example, [12]).

Alternatively, CCD systems with special optics to reduce the numerical aperture of the detector will also reject more scattered light [32].

Of course, avoiding scattering altogether is best of all. Other dosimeters such as the polyurethane-based Presage are being developed, which, like Fricke gel, employ absorption instead of scattering but are stable, not subject to diffusion. However, water–gel dosimeter materials such as gelatin are more tissue equivalent with respect to ionizing radiation [33] than plastics.

4. Conclusions

Although this model was very simple and developed to account for artifacts in the simpler layered finger phantom, it is still adequate to account for the artifacts evident in this more complex phantom. The artifacts can be accounted for entirely by the effects of scattering and the presence of scattered stray light. This emphasizes the importance of taking into account scattered stray light when reconstructing projections obtained using a CCD camera in cone beam optical CT.

The simple assumption of horizontally uniform stray light in each region of the image accurately fits the optical behavior, probably in part because of the simple geometry and high symmetry of the phantom. Although the model fails in the penumbra near the boundary of the inner/outer fields of the highest Δ layers in the projection images, this can also be rationalized qualitatively as an effect of scattering.

However, a model assuming this simple behavior of scattered stray light will not, in general, be useful in reconstructing realistic dose profiles in real dosimeters. A more sophisticated reconstruction algorithm that includes a model for optical scattering could mitigate the observed artifacts in more general cases.

References

1. C. Baldock, "Historical overview of the development of gel dosimetry: a personal perspective," J. Phys. Conf. Ser. **56**, 14–22 (2006).
2. J. Trapp, S. Å. J. Bäck, M. Lepage, G. Michael, and C. Baldock, "An experimental study of the dose response of polymer gel dosimeters imaged with x-ray computed tomography," Phys. Med. Biol. **46**, 2939–2951 (2001).
3. J. C. Gore, M. Ranade, M. J. Maryanski, and R. J. Schulz, "Radiation dose distributions in three dimensions from tomographic optical density scanning of polymer gels. I. Development of an optical scanner," Phys. Med. Biol. **41**, 2695–2704 (1996).
4. M. J. Maryanski, J. C. Gore, R. P. Kennan, and R. J. Schulz, "NMR relaxation enhancement in gels polymerized and cross-linked by ionizing radiations: a new approach to 3-D dosimetry by MRI," Magn. Reson. Imaging **11**, 253–258 (1993).
5. M. L. Mather and C. Baldock, "Ultrasound tomography imaging of radiation dose distributions in polymer gel dosimeters: preliminary study," Med. Phys. **30**, 2140–2148 (2003).
6. L. J. Schreiner, "Dosimetry in modern radiation therapy: limitations and needs," J. Phys. Conf. Ser. **56**, 1–13 (2006).
7. A. J. Venning, K. N. Nitschke, P. J. Keall, and C. Baldock, "Radiological properties of normoxic polymer gel dosimeters," Med. Phys. **32**, 1047–1053 (2005).
8. S. Brown, A. Venning, Y. De Deene, P. Vial, L. Oliver, J. Adamovics, and C. Baldock, "Radiological properties of the PRESAGE and PAGAT polymer dosimeters," Appl. Radiat. Isot. **66**, 1970–1974 (2008).
9. J. G. Wolodzko, C. Marsden, and A. Appleby, "CCD imaging for optical tomography of gel radiation dosimeters," Med. Phys. **26**, 2508–2513 (1999).
10. M. Oldham, J. H. Siewerdsen, A. Shetty, and D. A. Jaffray, "High resolution gel-dosimetry by optical-CT and MR scanning," Med. Phys. **28**, 1436–1445 (2001).
11. S. J. Doran and N. Krstajić, "The history and principles of optical computed tomography for scanning 3-D radiation dosimeters," J. Phys. Conf. Ser. **56**, 45–57 (2006).
12. N. Krstajić and S. J. Doran, "Fast laser scanning optical-CT apparatus for 3D radiation dosimetry," Phys. Med. Biol. **52**, N257–N263 (2007).
13. H. S. Sakhalkar and M. Oldham, "Area detector based optical-CT scanner for 3D dosimetry," Med. Phys. **35**, 101–111 (2008).
14. H. Fricke and S. Morse, "The chemical action of roentgen rays on dilute ferrosulphate as a measure of dose," Am J Roentgenol Radium Ther **18**, 430–432 (1927).
15. B. L. Gupta and K. R. Gomathy, "Consistency of ferrous sulphate-benzoic acid-xylenol orange dosimeter," Int. J. Appl. Radiat. Isot. **25**, 509–513 (1974).
16. A. Appleby and A. Leghrouz, "Imaging of radiation dose by visible color development in ferrous-agarose-xylenol orange gels," Med. Phys. **18**, 309–312 (1991).
17. P. J. Harris, A. R. Piercy, and C. Baldock, "A method for determining the diffusion coefficient in Fe(II/III) radiation dosimetry gels using finite elements," Phys. Med. Biol. **41**, 1745–1753 (1996).
18. C. Baldock, P. J. Harris, A. R. Piercy, and B. Healy, "Experimental determination of the diffusion coefficient in two-dimensions in ferrous sulphate gels using the finite element method," Australas. Phys. Eng. Sci. Med. **24**, 19–30 (2001).
19. K. McAuley, "Fundamentals of polymer gel dosimeters," J. Phys. Conf. Ser. **56**, 35–44 (2006).
20. C. Baldock, R. P. Burford, N. Billingham, G. S. Wagner, S. Patval, R. D. Badawi, and S. F. Keevil, "Experimental procedure for the manufacture and calibration of polyacrylamide gel (PAG) for magnetic resonance imaging (MRI) radiation dosimetry," Phys. Med. Biol. **43**, 695–702 (1998).
21. A. J. Venning, B. Hill, S. Brindha, B. J. Healy, and C. Baldock, "Investigation of the PAGAT polymer gel dosimeter using magnetic resonance imaging," Phys. Med. Biol. **50**, 3875–3888 (2005).
22. M. Lepage, A. K. Whittaker, L. Rintoul, S. Å. J. Bäck, and C. Baldock, "Modelling of post-irradiation events in polymer gel dosimeters," Phys. Med. Biol. **46**, 2827–2839 (2001).
23. L. Wind and W. W. Szymanski, "Quantification of scattering corrections to the Beer–Lambert law for transmittance measurements in turbid media," Meas. Sci. Technol. **13**, 270–275 (2002).
24. Y. De Deene, P. Hanselaer, C. De Wagter, E. Achten, and W. De Neve, "An investigation of the chemical stability of a monomer/polymer gel dosimeter," Phys. Med. Biol. **45**, 859–878 (2000).
25. S. Bosi, P. Naseri, A. Puran, J. Davies, and C. Baldock, "Initial investigation of a novel light-scattering gel phantom for evaluation of optical CT scanners for radiotherapy gel dosimetry," Phys. Med. Biol. **52**, 2893–2903 (2007).
26. S. G. Bosi, S. Brown, S. Sarabipour, Y. De Deene, and C. Baldock, "Modelling optical scattering artefacts for varying pathlength in a gel dosimeter phantom," Phys. Med. Biol. **54**, 275–283 (2009).
27. J. Miller, J. Adamovics, and J. Dietrich, "Cone beam optical CT scanner for 3D dosimetry," Med. Phys. **32**, 2138 (2005).
28. L. A. Feldkamp, L. C. Davis, and J. W. Kress, "Practical cone–beam reconstruction," J. Opt. Soc. Am. A **1**, 612–619 (1984).
29. S. R. Arridge and J. C. Hebdenz, "Optical imaging in medicine. II. Modelling and reconstruction," Phys. Med. Biol. **42**, 841–853 (1997).
30. A. P. Gibson, J. C. Hebden, and S. R. Arridge, "Recent advances in diffuse optical imaging," Phys. Med. Biol. **50**, R1–R43 (2005).
31. M. Bertram, J. Wiegert, and G. Rose, "Scatter correction for cone-beam computed tomography using simulated object models," Proc. SPIE **6142**, doi:10.1117/12.651027 (2006).
32. H. S. Sakhalkar and M. Oldham, "Area detector based optical-CT scanner for 3D dosimetry," Med. Phys. **35**, 101–111 (2008).
33. S. Brown, A. Venning, Y. De Deene, P. Vial, L. Oliver, J. Adamovics, and C. Baldock, "Radiological properties of the PRESAGE and PAGAT polymer dosimeters," Appl. Radiat. Isot. **66**, 1970–1974 (2008).

Applied Optics

BACK TO RESULTS

Basic Description | Other Editions/ Formats | Abstracting/ Indexing & Article Access | Publisher & Ordering Information | Advertising, Rights, Demographics | Reviews

JCR Web

Click highlighted text for a new search on that item.

ISSN:	1559-128X
Title:	Applied Optics
Publishing Body:	Optical Society of America
Country:	United States
Status:	Active
Start Year:	2004
Frequency:	36 times a year
Document Type:	Journal; Academic/Scholarly
Refereed:	Yes
Abstracted/Indexed:	Yes
Media:	Print
Alternate Edition ISSN:	2155-3165
Size:	Standard
Language:	Text in English
Price:	USD 4,590 combined subscription per year domestic to institutions (Print & Online Eds.) USD 4,810 combined subscription per year in Canada to institutions (Print & Online Eds.) USD 5,075 combined subscription per year elsewhere to institutions (Print & Online Eds.) (effective 2010)
Subject:	PHYSICS - OPTICS
Dewey #:	535
LC#:	QC350
Special Features:	Includes Advertising, Charts, Illustrations, Patents, Abstracts, Book Reviews
Article Index:	Cum.index: vols.1-36
Editor(s):	Joseph N Mait (Editor-in-Chief)
E-Mail:	aomss@osa.org
URL:	http://www.opticsinfobase.org/ao/journal/ao/about.cfm

Additional Title Information

ADDITIONAL TITLE INFORMATION

Alternate Title:	Abbreviated title: A O
Title History:	Formed by the merger of (1990-2004): Applied Optics. Information Processing (United States) (1540-8973); (1995-2004): Applied Optics. Optical Technology and Biomedical Optics (United States) (1540-8981); (1991-2004): Applied Optics. Lasers, Photonics, and Environmental Optics (United States) (1540-899X); All of which superseded (1962-1990): Applied Optics (United States) (0003-6935)

Back to Top

Add this item to: (select a list) + ADD

Request this title:
I'd like to request this title. GO

Corrections:
Submit corrections to Ulrich's about this title. GO

Publisher of this title?
If yes, click GO! to contact Ulrich's about updating your title listings in the Ulrich's database. GO

Print • Download • E-mail

Back to Top